Protostellar Outflow Heating in a Growing Massive Protocluster

Ke Wang^{1,2}, Qizhou Zhang², Yuefang Wu¹, Hua-bai Li³, and Huawei Zhang¹

kwang@cfa.harvard.edu

ABSTRACT

The dense molecular clump P1 in the infrared dark cloud (IRDC) complex G28.34+0.06 harbors a massive protostellar cluster at its extreme youth. Our previous Submillimeter Array (SMA) observations revealed several jet-like CO outflows emanating from the protostars, indicative of intense accretion and potential interaction with ambient natal materials. Here we present the Expanded Very Large Array (EVLA) spectral line observations toward P1 in the NH₃ (J,K) = (1,1), (2,2), (3,3) lines, as well as H₂O and class I CH₃OH masers. Multiple NH₃ transitions reveal the heated gas widely spread in the 1 pc clump. The temperature distribution is highly structured; the heated gas is offset from the protostars, and morphologically matches the outflows very well. Hot spots of spatially compact, spectrally broad NH₃ (3,3) emission features are also found coincident with the outflows. A weak NH₃ (3,3) maser is discovered at the interface between an outflow jet and the ambient gas. These findings suggest that protostellar heating may not be effective in suppressing fragmentation during the formation of massive cores.

Subject headings: ISM: individual (G28.34+0.06) — ISM: jets and outflows — ISM: magnetic fields — stars: formation — stars: early-type — masers

1. Introduction

The majority of stars, from low to high mass ones are born in clusters (Lada & Lada 2003). In a clustered environment, feedback from protostellar radiation and outflows can

¹Department of Astronomy, School of Physics, Peking University, Beijing 100871, China

²Harvard-Smithsonian Center for Astrophysics, 60 Garden Street, Cambridge MA 02138, USA

³Max-Planck Institute for Astronomy, Königstuhl 17, D-69117 Heidelberg, Germany

play an important role in shaping their parental molecular cloud and thereby regulate further cloud fragmentation and star formation. In particular, protostellar feedback may be crucial for the formation of massive stars which typically contain masses at least one order of magnitude higher than the global Jeans mass in the molecular clump ($M_J \sim 1 M_{\odot}$ for $n_{\rm H} \sim 10^5$ cm⁻³ and $T \sim 15$ K; Pillai et al. 2006; Rathborne et al. 2006). Calculations have shown that the accretion luminosity of a low mass protostar can heat gas to 100 K out to hundreds of AU, thereby raising the local thermal Jeans mass (Masunaga & Inutsuka 2000; Krumholz 2006). Subsequent numerical simulations indicate that protostellar heating from low mass stars in the cluster may change the equation of state (Larson 1985), and suppress the fragmentation (Krumholz et al. 2010), thereby aiding the formation of massive cores. On the other hand, protostellar outflows in the cluster can also inject momentum and energy into the local medium, and affect the evolution of the cloud (Quillen et al. 2005; Curtis et al. 2010; Wang et al. 2010).

To investigate the protostellar feedback, we observed the dense molecular clump P1 in the IRDC complex G28.34+0.06. Located in the southern part of G28.34+0.06, P1 is one of the dense molecular clumps among the filamentary network in the IRDC complex which stretches over 6 pc at a kinematic distance of 4.8 kpc (Carey et al. 2000; Rathborne et al. 2006; Wang et al. 2008). P1 is a northeast-southwest (NE-SW) orientated molecular clump containing a large mass reservoir of $10^3 M_{\odot}$ within a size of 1 pc. Wang et al. (2008) presented an NH₃ mosaic of the entire IRDC, and found that the gas temperature decreases from 20 to 14 K toward the inner part of P1, indicative of external heating. A similar trend was found in the NH_3 line width, suggesting a turbulence dissipation toward smaller scales. Our SMA observations resolved the P1 clump into a string of five cores (named SMA1-5) containing 22-64 M_{\odot} in mass and ≤ 0.1 pc in size; at higher angular resolution and better sensitivity, the cores are further resolved into ten compact condensations (named, e.g. SMA2a–d) with masses of 1.4–10.6 M_{\odot} and sizes of ~0.01 pc, indicative of a hierarchical fragmentation (Zhang et al. 2009; Wang et al. 2011). In addition, all five cores are associated with highly collimated CO (3–2) outflows. The large mass reservoir and the ongoing accretion indicate that P1 will eventually form a massive star cluster after the accretion is completed. This young protocluster provides an opportunity to investigate how protostellar heating and outflows affect the parent molecular environment, and the formation of massive cores. The new EVLA observations presented in this Letter reveal the temperature profiles at unprecedented high angular resolution, allowing us to evaluate the protostellar feedback in detail.

2. Observations

The NRAO¹ EVLA was used to obtain the NH₃ (J,K) = (1,1), (2,2), (3,3), as well as H₂O and CH₃OH maser line emission data in 2010 during the EVLA early science phase. Table 1 summarizes the observations. The data were calibrated in CASA² and imaged using CASA and Miriad³.

The NH₃ (1,1) and (2,2) observed in the EVLA C array has a channel width of 0.2 km s⁻¹. Wang et al. (2008) observed NH₃ (1,1) and (2,2) toward the same phase center in the VLA D array with a channel spacing of 0.6 km s⁻¹. We combined the calibrated visibilities of Wang et al. (2008) with the new C array data for imaging. To increase the signal-to-noise ratio in the final images, we averaged the channel width to 0.3 km s⁻¹ and tapered the visibilities with a Gaussian function with a FWHM of 180 k λ . We also made images with a 0.6 km s⁻¹ channel width to compare with the images at 0.3 km s⁻¹ resolution, and found that the latter does not introduce additional features. For the NH₃ (3,3) images we also averaged the channel width to 0.3 km s⁻¹ to improve the signal-to-noise ratio.

3. Results

3.1. Ammonia Emission

Figure 1 presents moment 0, 1 and 2 maps of the NH₃ (1,1), (2,2) and (3,3) main hyperfine emission. The NE-SW orientated filament is traced by the NH₃ (1,1) and (2,2) emission extremely well. Ammonia cores coincide with all the SMA dust cores, indicating that NH₃ traces the dense envelopes of the protostellar cores. As illustrated in the moment 1 images of NH₃ (1,1) and (2,2), there is a velocity gradient of 1.5 km s⁻¹ over 1 pc along the filament. This gradient is, however, not uniform; it is enhanced toward southwest starting at SMA5. On the other hand, the velocity field from SMA1 through SMA4 is quite uniform, at about 79 km s⁻¹. The moment 2 images show similar velocity dispersion⁴ of 0.4–0.8 km s⁻¹ along the filament as traced by NH₃ (1,1) and (2,2). The velocity dispersion is enhanced to several local maxima of 0.6–0.8 km s⁻¹ which coincide with all the SMA dust cores except

¹The National Radio Astronomy Observatory is a facility of the National Science Foundation operated under cooperative agreement by Associated Universities, Inc.

² http://casa.nrao.edu

³ http://www.astro.umd.edu/~teuben/miriad, http://www.cfa.harvard.edu/sma/miriad

⁴For a Gaussian line profile, velocity dispersion σ is related to FWHM line width ΔV as $\sigma = \Delta V/2\sqrt{2\ln 2}$.

SMA3. The enhancements may originate from a combination of spatially unresolved motions such as rotation, infall, and outflow.

In addition to the main filament, the NH₃ (1,1) emission also reveals a fainter northwestsoutheast (NW-SE) orientated filament, crossing the main filament at SMA5, making an X shape. This minor filament is located at a slightly different velocity, around 82 km s⁻¹. Compared to the main filament, the minor filament shows weaker emission in NH₃ (1,1) and little emission in NH₃ (2,2), indicative of even colder gas. The minor filament is evident in the previous NH₃ (1,1) image at lower resolution (Wang et al. 2006; Zhang et al. 2009), however, it does not correspond to any dust emission feature at 350–1300 μ m (Rathborne et al. 2006, 2010; Zhang et al. 2009; Chen et al. 2010; Wang et al. 2011). Therefore, the minor filament is remarkably less dense than the main filament. Like the main filament, the minor filament consists of a velocity gradient of 2 km s⁻¹ over 1 pc; it also hosts several NH₃ cores with sizes similar to the NH₃ cores on the main filament. It has a velocity dispersion of ≤ 0.4 km s⁻¹ in general, but local enhancements of up to 0.5 km s⁻¹ are also presented. We will discuss the nature of the minor filament in Section 4.3. In the following text, unless otherwise stated, we refer the main NE-SW filament as "the filament".

It is interesting to note that the clumpy NH₃ (3,3) emission does not follow the dust filament at all. We visually identified five representative peaks from the (3,3) moment 0 map, labeled as A–E in Figure 1. None of these peaks coincide with any dust cores. In fact, the only one that lies on the filament is peak D which is between SMA4 and SMA5; other peaks are offset from the filament. Because NH₃ (3,3) is excited at an energy level of 125 K, these ammonia peaks trace local temperature enhancements relative to the generally cold molecular clump. Another important feature is the large velocity dispersion: all the peaks show centrally condensed distribution of $\sigma > 0.8$ km s⁻¹, and up to 2.2 km s⁻¹ in peak B. Peak B is located down stream of the red lobe of outflow SMA2a, the most energetic outflow in P1 (Wang et al. 2011). The centroid velocity on peak B is redshifted relative to the filament, consistent with the redshifted CO emission. Indeed, all these NH₃ (3,3) peaks seem to trace the footprint of the jet-like CO (3–2) outflows revealed by the SMA (Wang et al. 2011). We will discuss this further in Section 4.1.

3.2. Maser Emission

We report maser detections based on the following criteria: (a) Peak flux $\geq 6\sigma$; (b) Emission continues at least two channels with flux $\geq 4\sigma$; and (c) Within the primary beam response of ≥ 0.3 . We adopt these criteria because at some channels the images are contaminated by the side lobes of a strong maser located at P2, well outside of the primary beam. Using the criteria, we identify 4 water masers (W1–4) and 1 methanol maser (M1), as presented in Figure 2. Positions of the masers are obtained by fitting a two dimensional Gaussian to the brightness distribution of the maser emission. The positional uncertainty is $\leq 0''.02$. All masers are either coincident with or close to infrared point sources at 8–24 μ m.

Comparing the maser positions and velocities with previous observations made with VLA (Wang et al. 2006, resolution $\sim 2''$) and GBT (Chambers et al. 2009, resolution $\sim 30''$), we find that W1, W3, and W4 are new features, while W2 and M1 are spatially and spectrally coincident with two masers reported before. Both W2 and M1 have been varying in peak flux during the last several years: W2 was 2.4 Jy on 2005 September 23/24, then brightened to 6 Jy on 2006 December 5, and dimmed dramatically to 0.03 Jy on 2010 November 24; M1 dimmed from 0.24 Jy on 2006 December 5 to 0.02 Jy on 2010 November 24. On the other hand, W1 and W3 were either newly emerged or experienced brightening between 2006 and 2010, otherwise they should have been detected by Chambers et al. (2009). W4 is below the detection limit of Chambers et al. (2009).

Among all the five detected masers, only two (W1, W2) are associated with NH₃ emission above 6σ significance. W1 and W2 locate right on top of the dust condensations SMA2a and SMA2b, respectively, and thus are presumably excited by the protostars embedded in the same dust condensations. The position discrepancy between the H₂O maser with its exciting protostar is within a fraction of 1000 AU.

4. Discussion

4.1. Outflow Heating

Intensity ratios of the main and hyperfine components from multiple NH₃ (J,K) transitions constrain rotational temperature which well approximates kinetic temperature in the regime of <20 K (Ho & Townes 1983; Walmsley & Ungerechts 1983). In the following analysis, we assume that the rotational temperature is the same as the kinetic temperature when the former is <20 K. Following the procedure of Ho & Townes (1983), we compute a rotational temperature (T_{21}) map based on the NH₃ (1,1) and (2,2) images. The NH₃ images were first smoothed to a common beam of 2".8 before computing the T_{21} map. The uncertainty of T_{21} is estimated to be 3 K. Figure 3(a) shows T_{21} with the dust condensations and the CO (3–2) outflows superposed. The T_{21} map reveals a highly structured temperature profile ranging from 8 to 30 K, opposite to the smooth temperature profiles observed in other IRDCs (Ragan et al. 2011). This may be due to beam dilution since the data in Ragan et al. (2011) have a larger beam. A number of remarkable enhancements ($T_{21} > 26$ K) are present among the entire map, but surprisingly none of the temperature enhancements coincide with any dust condensations. Instead, all the T_{21} enhancements spatially match the footprint of the outflows.

Since the NH_3 (3,3) is more widely spread than the (1,1) toward the northwest where the signal-to-noise ratio of (1,1) prohibits us from computing opacity, it is difficult to derive a reliable rotational temperature map from the NH_3 (1,1) and (3,3) lines. Instead, we compute the intensity ratio of the main hyperfine of (3,3)/(1,1), R_{31} , as plotted in Figure 3(b). To compute the intensity ratio, the NH_3 (1,1) image was first smoothed to the beam of the (3,3) image. The intensity ratio is positively correlated with the rotational temperature (Ho & Townes 1983; Zhang et al. 2002). For reference, assuming optically thin emission and the same abundance for the ortho and para NH_3 (Zhang et al. 2007), $R_{31} = 0.5$, 2, and 5 correspond to rotational temperatures of $T_{31} = 31, 55$, and 109 K, respectively. Like the T_{21} map, the R_{31} map is also highly structured. R_{31} varies continuously from 0.3 to 12.5 over the map. Again several hot spots represented by R_{31} peaks (corresponding to NH₃ (3,3) emission peaks A–E) match the outflow footprint and are offset from the dust condensations. In addition to the peaks, there is a low R_{31} valley along SMA2 to SMA3. Optically thin thermal NH₃ (3,3) emission should have $R_{31} \leq 6.4$ (Ho & Townes 1983). Higher R_{31} values are seen toward peaks A–C, indicative of non-thermal emission. Toward peak B, the (3,3) emission is weakly amplified (Figure 4), resembling an NH_3 (3,3) maser similar to those found in other massive star formation regions where outflows are present (e.g. Mangum & Wootten 1994; Zhang & Ho 1995; Beuther et al. 2007; Brogan et al. 2011). However the spatial resolution is insufficient to constrain the brightness of this emission feature.

The morphological match between the heated gas and the outflow footprint suggests that the heating in the P1 region is due to protostellar outflows. Indeed, all the hot spots exclusively coincide with large NH₃ (3,3) line widths compared to relatively small line width toward the dust condensations (Figure 4), likely indicative of gas motion and extra turbulence injected by the outflow shocks. The outflow heating has two important features. First, the heating alters thermal property of the gas throughout the clump, from a distance 0.1 pc up to 0.5 pc away from the driving protostars. Second, the heating is localized and far from well mixed. The temperature at the low R_{31} valley is not high enough to suppress further fragmentation into Jeans mass of 1 M_{\odot} (Wang et al. 2011). We probably have witnessed through EVLA and SMA the very beginning of an outflow induced gas heating.

4.2. Radiative Heating

It is apparent that protostellar outflows can introduce significant heating to the ambient gas. What is the effect of protostellar radiation? Is radiative heating from low mass protostars sufficient to suppress fragmentation and aid the formation of massive cores? The fact that all dense cores correspond with low R_{31} is intriguing. In addition, the temperature map in Figure 3(a) indicates that dense cores have typical temperatures of 18 K, and are offset from the high temperature peaks. The temperature distributions suggest that the heating of low mass protostars may not play a significant role in the formation of dense cores detected with the SMA. Otherwise, massive cores should be found at the peaks of the temperature distribution. Longmore et al. (2011) made a similar statement for a hot molecular core G8.68–0.37.

It is also interesting to note that the protostars embedded in the SMA cores have not produced significant heating. SMA1 to SMA4 have a rather uniform T_{21} of 18 K, while SMA5 has a lower T_{21} of 9 K. We caution that the T_{21} map has a 2".8 beam, so any temperature structure has been smoothed to a spatial scale of 0.065 pc. How much luminosity is required to heat the gas to 18 or 9 K at a radius of 0.065 pc from the central source? Assuming thermal equilibrium between gas and dust, the luminosity can be estimated following the equation (Scoville & Kwan 1976; Garay & Lizano 1999):

$$T_{\rm dust} = 65 \left(\frac{0.1\,{\rm pc}}{r}\right)^{2/(4+\beta)} \left(\frac{L_{\rm star}}{10^5 L_{\odot}}\right)^{1/(4+\beta)} \left(\frac{0.1}{f}\right)^{1/(4+\beta)} \,,$$

where $\beta = 1.5$ is the dust emissivity at far infrared wavelengths (Rathborne et al. 2010), $f = 0.08 \,\mathrm{cm^2 \, g^{-1}}$ is the dust emissivity at 50 $\mu\mathrm{m}$ (Scoville & Kwan 1976), and r = 0.065pc is the radius from the central protostar. We estimate a luminosity of 30 L_{\odot} for each protostar embedded in SMA1, SMA2a, SMA3, and SMA4a, and 1 L_{\odot} for the protostar SMA5. These values should be taken with caution because the beam dilution may introduce large uncertainty in both temperature and radius. Nevertheless, we note that the luminosity of SMA2a is in rough agreement with the luminosity inferred from SED for the 24 $\mu\mathrm{m}$ source in the SMA2 vicinity ($\sim 10^2 L_{\odot}$, Wang et al. 2008). A lack of significant heating from the growing protostars is consistent with non detection of line emission from organic molecules (Zhang et al. 2009; Wang et al. 2011).

4.3. Origin of the Minor Filament

The origin of the low-density minor filament is rather interesting. A low-density streak perpendicular to a high-density oblate region is expected if magnetic field is dynamically important compared to self-gravity and turbulence during the formation of the system (Li et al. 2011). In this case, gravitational contraction along the field lines is more efficient, resulting in a high-density region perpendicular to the magnetic field, while on the other hand turbulence is also channeled by the field and gives rise to streaks aligned with the magnetic field in the lower-density region. This phenomenon has been seen in simulations (Price & Bate 2008; Nakamura & Li 2008) and in observations of NGC 2024 in Orion (Li et al. 2011). In G28.34-P1, the X-shaped filamentary system projected on the sky is almost perpendicular. If the system were formed from the same mechanism, one should expect a mean magnetic field along the minor filament and perpendicular to the main filament. Based on the JCMT dust polarization data cataloged by Matthews et al. (2009), we derived a mean B-field direction of P.A. = $-25^{\circ}.6 \pm 45^{\circ}$ as labeled on Figure 1. Because the main filament has a P.A. of 48° (Wang et al. 2011), the separation angle between the mean B-field and the main filament is $73^{\circ}.6$. The mean magnetic field at the clump scale is indeed along with the minor filament and roughly perpendicular to the main filament. The large deviation in the B-field direction may indicate that the strong outflows have started to disturb the initially ordered field lines in the inner part of P1 (Li et al. 2009). Therefore we speculate that the minor filament originates from turbulence anisotropy during the formation of the X-shaped filamentary system, and that the formation process has been governed by the interplay between strong magnetic field, self-gravity, and turbulence.

We thank Edward T. Chambers for providing the spectra of the masers detected in G28.34+0.06. K.W. acknowledges the support from the SMA predoctoral fellowship and the China Scholarship Council. Q.Z. acknowledges the support from the Smithsonian Institution Endowment Funds. This research was supported in part by the NSFC grants 10733030, 10873019 and 11073003.

Facilities: EVLA

Parameter/Line	NH_3 (1,1)	NH_3 (2,2)	NH_3 (3,3)	$\rm H_2O/CH_3OH$
Observing date	2010Oct09	2010Oct11	2010May09	2010Nov24
Configuration	\mathbf{C}	\mathbf{C}	D	С
Rest frequency (GHz)	23.694	23.722	23.870	22.235/24.959
Primary beam (')	2	2	2	2
Gain calibrator	J1851 + 005	J1851 + 005	J1851 + 005	J1851 + 005
Flux calibrator ^a	3C48	3C48	3C48	3C48
Bandpass calibrator	3C454.3	3C454.3	3C454.3	3C454.3
Phase center ^b	Ι	Ι	II	II
Integration time (minute)	95	95	21	15/15
Bandwidth (MHz)	4	4	4	4
Polarization	dual	dual	dual	full
Naive channel width (km s^{-1})	0.2	0.2	0.2	0.8
Final channel width (km s^{-1})	0.3	0.3	0.3	0.8
Synthesized beam (") ^c	2.7×2.2	2.8×2.0	4.8×2.7	$1.3 \times 1.0 / 1.5 \times 0.9$
RMS noise (mJy/beam) ^d	1.2 - 1.5	1.2 - 1.5	3	1.2 - 1.5 / 0.8
Convention factor (K/Jy)	367	388	165	1939/1484
Weighting method	natural	natural	natural	robust/natural

 Table 1.
 Observational Parameters

^aAbsolute flux is accurate to about 5%.

^bPhase center I at (R.A., decl.)_{J2000} = $18^{h}42^{m}50^{s}$, $-04^{\circ}03'30''$; II at $18^{h}42^{m}50^{s}$.82, $-04^{\circ}03'11''$.3.

^cFinal NH₃ (1,1) and (2,2) images are made by adding archival D array data (Section 2).

 $^{\rm d}1\sigma$ rms noise measured in final images.

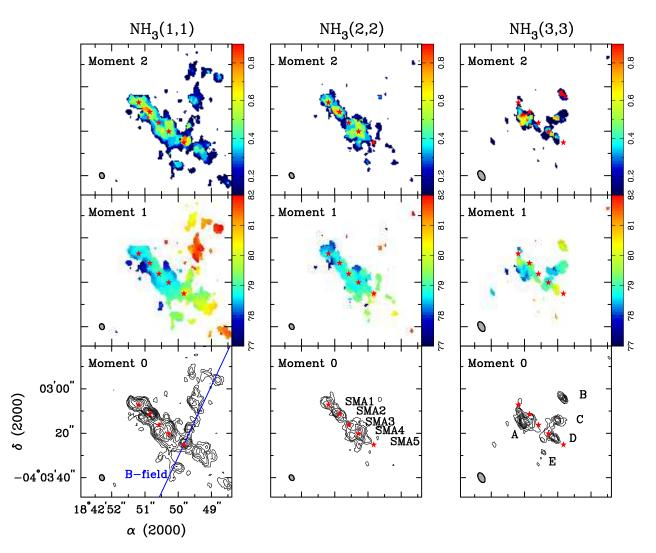


Fig. 1.— Moment maps of the main hyperfine emission of NH₃ (1,1), (2,2) and (3,3), shown on the left, middle and right columns, respectively. The contours are plotted in steps of 6σ , which is 0.5 mJy beam⁻¹ km s⁻¹ for (1,1) and (2,2), while 1 mJy beam⁻¹ km s⁻¹ for (3,3). Units of the color bars are km s⁻¹. The stars mark the five dust cores (SMA1–5) which are further resolved into smaller condensations (the black contours in Figure 3). The blue line on the bottom-left panel indicates the direction of the mean magnetic field (Section 4.3). The filled ellipses on the bottom-left corners represent synthesized beams.

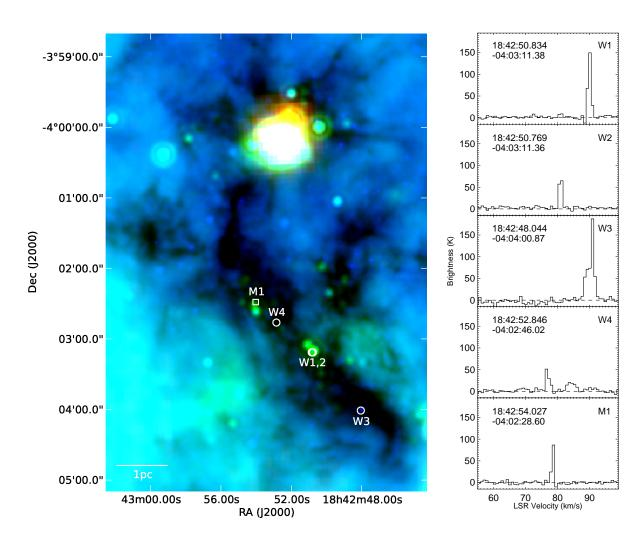


Fig. 2.— Detected water (W1–4) and methanol (M1) masers. Left: *Spitzer* composite image (red/green/blue = $70/24/8 \ \mu$ m) showing the IRDC G28.34+0.06 complex overlaid with the locations of the masers. The *Spitzer* data are taken from the GLIMPSE and MIPSGAL legacy projects (Churchwell et al. 2009; Carey et al. 2009). Right: Spectra of the masers. Brightness temperatures are corrected for primary beam response.

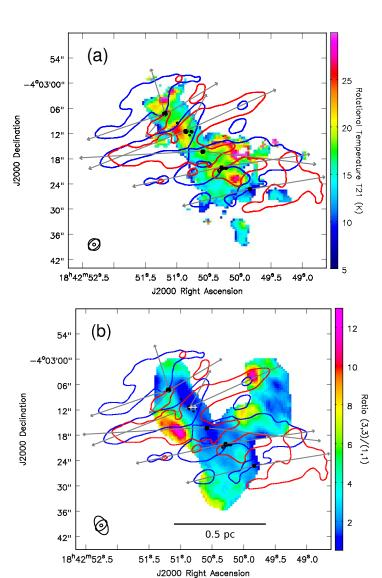


Fig. 3.— Morphological match between heated gas and protostellar outflows. Plotted in color scales are (a) T_{21} , the rotational temperature derived from NH₃ (1,1) and (2,2), and (b) R_{31} , the integrated intensity ratio of NH₃ (3,3)/(1,1). The arrows and blue/red contours outline the blue-/redshifted CO (3–2) outflows, and the compact black contours represent the five groups of dust condensations, SMA1–5, from upper-left to bottom-right (Wang et al. 2011). The two white crosses on top of SMA2a and SMA2b represent water masers W1 and W2, respectively. On the bottom-left corners are the beams for dust continuum, CO (3–2), and T_{21} (R_{31}), from the smallest to the largest respectively. Note that masks of 5σ were applied to both maps, and additional manual clipping was also performed to R_{31} in order to avoid noisy edge pixels.

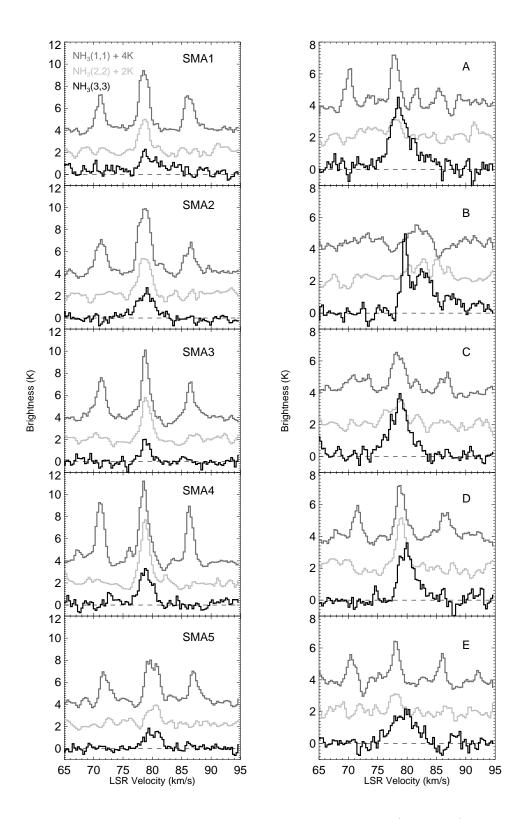


Fig. 4.— EVLA NH₃ spectra extracted from SMA dust peaks (SMA1–5) and NH₃ (3,3) peaks (A–D). Note at peak B a spectroscopically unresolved NH₃ (3,3) maser at about 84 km s⁻¹. (Panel E was truncated in formal publication due to the space limit of ApJ Letters.)

REFERENCES

- Beuther, H., Walsh, A. J., Thorwirth, S., Zhang, Q., Hunter, T. R., Megeath, S. T., & Menten, K. M. 2007, A&A, 466, 989
- Brogan, C. L., Hunter, T. R., Cyganowski, C. J., Friesen, R. K., Chandler, C. J., & Indebetouw, R. 2011, ApJ, 739, L16+
- Carey, S. J., Feldman, P. A., Redman, R. O., Egan, M. P., MacLeod, J. M., & Price, S. D. 2000, ApJ, 543, L157
- Carey, S. J., et al. 2009, PASP, 121, 76
- Chambers, E. T., Jackson, J. M., Rathborne, J. M., & Simon, R. 2009, ApJS, 181, 360
- Chen, H., Liu, S., Su, Y., & Zhang, Q. 2010, ApJ, 713, L50
- Churchwell, E., et al. 2009, PASP, 121, 213
- Curtis, E. I., Richer, J. S., Swift, J. J., & Williams, J. P. 2010, MNRAS, 408, 1516
- Garay, G., & Lizano, S. 1999, PASP, 111, 1049
- Ho, P. T. P., & Townes, C. H. 1983, ARA&A, 21, 239
- Krumholz, M. R. 2006, ApJ, 641, L45
- Krumholz, M. R., Cunningham, A. J., Klein, R. I., & McKee, C. F. 2010, ApJ, 713, 1120
- Lada, C. J., & Lada, E. A. 2003, ARA&A, 41, 57
- Larson, R. B. 1985, MNRAS, 214, 379
- Li, H.-B., Blundell, R., Hedden, A., Kawamura, J., Paine, S., & Tong, E. 2011, MNRAS, 411, 2067
- Li, H.-b., Dowell, C. D., Goodman, A., Hildebrand, R., & Novak, G. 2009, ApJ, 704, 891
- Longmore, S. N., Pillai, T., Keto, E., Zhang, Q., & Qiu, K. 2011, ApJ, 726, 97
- Mangum, J. G., & Wootten, A. 1994, ApJ, 428, L33
- Masunaga, H., & Inutsuka, S.-i. 2000, ApJ, 531, 350
- Matthews, B. C., McPhee, C. A., Fissel, L. M., & Curran, R. L. 2009, ApJS, 182, 143

- Nakamura, F., & Li, Z.-Y. 2008, ApJ, 687, 354
- Pillai, T., Wyrowski, F., Carey, S. J., & Menten, K. M. 2006, A&A, 450, 569
- Price, D. J., & Bate, M. R. 2008, MNRAS, 385, 1820
- Quillen, A. C., Thorndike, S. L., Cunningham, A., Frank, A., Gutermuth, R. A., Blackman, E. G., Pipher, J. L., & Ridge, N. 2005, ApJ, 632, 941
- Ragan, S. E., Bergin, E. A., & Wilner, D. 2011, ApJ, 736, 163
- Rathborne, J. M., Jackson, J. M., Chambers, E. T., Stojimirovic, I., Simon, R., Shipman, R., & Frieswijk, W. 2010, ApJ, 715, 310
- Rathborne, J. M., Jackson, J. M., & Simon, R. 2006, ApJ, 641, 389
- Scoville, N. Z., & Kwan, J. 1976, ApJ, 206, 718
- Walmsley, C. M., & Ungerechts, H. 1983, A&A, 122, 164
- Wang, K., Zhang, Q., Wu, Y., & Zhang, H. 2011, ApJ, 735, 64
- Wang, P., Li, Z.-Y., Abel, T., & Nakamura, F. 2010, ApJ, 709, 27
- Wang, Y., Zhang, Q., Pillai, T., Wyrowski, F., & Wu, Y. 2008, ApJ, 672, L33
- Wang, Y., Zhang, Q., Rathborne, J. M., Jackson, J., & Wu, Y. 2006, ApJ, 651, L125
- Zhang, Q., & Ho, P. T. P. 1995, ApJ, 450, L63+
- Zhang, Q., Hunter, T. R., Sridharan, T. K., & Ho, P. T. P. 2002, ApJ, 566, 982
- Zhang, Q., Sridharan, T. K., Hunter, T. R., Chen, Y., Beuther, H., & Wyrowski, F. 2007, A&A, 470, 269
- Zhang, Q., Wang, Y., Pillai, T., & Rathborne, J. 2009, ApJ, 696, 268

^{– 15 –}

This preprint was prepared with the AAS IATEX macros v5.2.